# *Plausible drying and wetting scenarios for summer in southeastern South America*

# Plausible Drying and Wetting Scenarios for Summer in Southeastern South America

JULIA MINDLIN,[a,b,c] CAROLINA S. VERA,[a,b,c] THEODORE G. SHEPHERD,[d] AND MARISOL OSMAN[b,c,e]

[a] *Departamento de Ciencias de la Atmósfera y los Océanos, Facultad de Ciencias Exactas y Naturales, Universidad de Buenos Aires, Buenos Aires, Argentina*
[b] *Centro de Investigaciones del Mar y la Atmósfera, Consejo Nacional de Investigaciones Científicas y Técnicas, Universidad Nacional de Buenos Aires, Buenos Aires, Argentina*
[c] *Instituto Franco Argentino sobre Estudios de Clima y Sus Impactos (IFAECI-UMI3351), Centre National de la Recherche Scientifique, Buenos Aires, Argentina*
[d] *Department of Meteorology, University of Reading, Reading, United Kingdom*
[e] *Institute of Meteorology and Climate Research, Department of Troposphere Research (IMK–TRO), Karlsruhe Institute of Technology, Karlsruhe, Germany*

(Manuscript received 8 March 2023, in final form 14 August 2023, accepted 23 August 2023)

ABSTRACT: Summer rainfall trends in southeastern South America (SE-SA) have received attention in recent decades because of their importance for climate impacts. More than one driving mechanism has been identified for the trends, some of which have opposing effects. It is still not clear how much each mechanism has contributed to the observed trends or how their combined influence will affect future changes. Here, we address the second question and study how the CMIP6 summer SE-SA rainfall response to greenhouse warming can be explained by mechanisms related to large-scale extratropical circulation responses in the Southern Hemisphere to remote drivers (RDs) of regional climate change. We find that the regional uncertainty is well represented by combining the influence of four RDs: tropical upper-tropospheric amplification of surface warming, the delay in the stratospheric polar vortex breakdown date, and two RDs characterizing recognized tropical Pacific SST warming patterns. Applying a storyline framework, we identify the combination of RD responses that lead to the most extreme drying and wetting scenarios. Although most scenarios involve wetting, SE-SA drying can result if high upper-tropospheric tropical warming and early stratospheric polar vortex breakdown conditions are combined with low central and eastern Pacific warming. We also show how the definition of the SE-SA regional box can impact the results since the spatial patterns characterizing the dynamical influences are complex and the rainfall changes can be averaged out if these are not considered when aggregating. This article's perspective and the associated methodology are applicable to other regions of the globe.

SIGNIFICANCE STATEMENT: Summer rainfall in southeastern South America (SE-SA) affects an area where around 200 million people live. The observed trends suggest long-term wetting, and most climate models predict a wetting response to greenhouse warming. However, in this work, we find that there is a physically plausible combination of large-scale circulation changes that can promote drying, which means SE-SA drying is a possibility that cannot be ignored. We also show that the definition of the SE-SA regional box can impact regional rainfall analysis since the spatial patterns characterizing the dynamical influences are complex and the changes can be averaged out if these are not considered when aggregating. This perspective and the associated methodology are applicable to other regions of the globe.

KEYWORDS: Atmospheric circulation; Climate change; Uncertainty

## 1. Introduction

Southeastern South America (SE-SA) is a region where large summer rainfall trends have been recorded and attributed at least in part to human influence (e.g., Barros et al. 2000; Vera and Díaz 2015; Saurral et al. 2017; Díaz et al. 2021). SE-SA covers the total extent of La Plata basin, the second-largest hydrological basin in South America. The region has a large and locally dense population that to a large extent relies on agricultural activities and hydroenergy production. Agricultural activities have expanded over the basin, mainly due to the increase in food demand (Schlindwein et al. 2021), and have been favored at least partially by upward summer rainfall trends in the past decades (Zak et al. 2008). Van Garderen and Mindlin (2022) showed that recent summer droughts could have been more severe if it had not been for the wetting trend of the last decades (1960–present) associated with 1°C warming.

More than one driving mechanism has been identified for summer rainfall trends in SE-SA, some of which have opposing effects at the same time range (Junquas et al. 2013; Gonzalez et al. 2014; Saurral et al. 2017; Zilli et al. 2019; Mindlin et al. 2020, hereafter M20; Doblas-Reyes et al. 2021). Moreover, the effect of ozone recovery combined with greenhouse gas (GHG)

Denotes content that is immediately available upon publication as open access.

Supplemental information related to this paper is available at the Journals Online website: https://doi.org/10.1175/JCLI-D-23-0134.s1.

*Corresponding author*: Theodore G. Shepherd, theodore.shepherd@reading.ac.uk

DOI: 10.1175/JCLI-D-23-0134.1

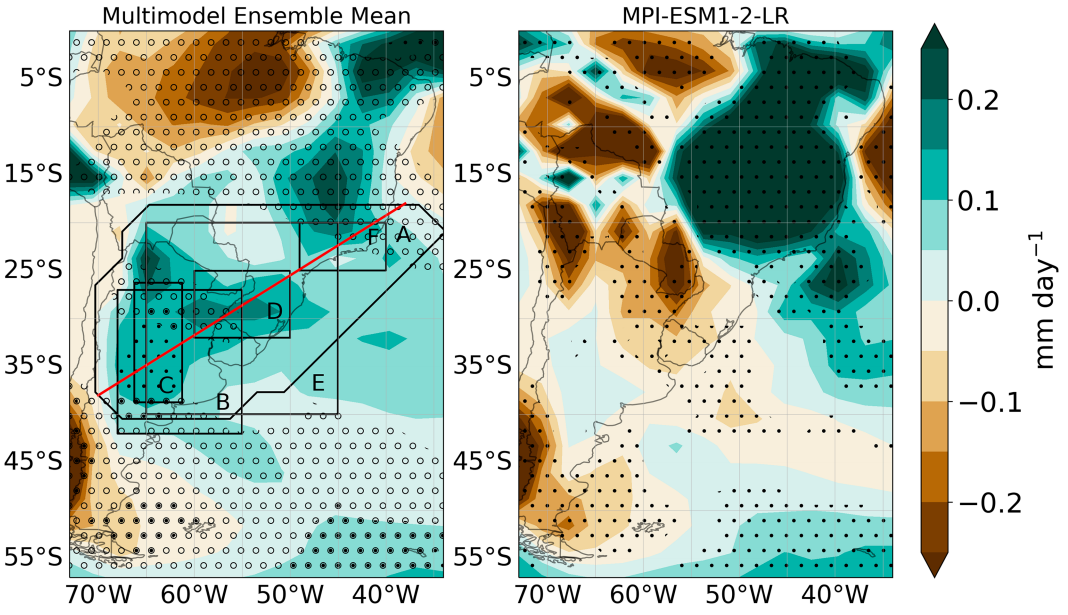


FIG. 1. Summer mean precipitation change by the end of the century (2070–99) with respect to the recent past (1990–2019) in the SSP5-8.5 scenario. (a) Multimodel ensemble mean. Full stippling shows where at least 90% of models agree on the sign of the change, and open stippling [following Zappa et al. (2021)] indicates where individual models show a large response compared to year-to-year variability. Therefore, full stippling with circles shows where both occur, whereas just open stippling shows a potentially large response compared to year-to-year variability in the presence of a nonrobust projection. (b) Response for the model MPI-ESM1-2-LR. Stippling shows regions where at least 9 of the 10 ensemble members show a signal-to-noise ratio ($\gamma$) larger than 1 (see text for details of the signal-to-noise diagnostics). The regional boxes in (a) indicate regions used to evaluate aggregated precipitation in previous works, namely, in the IPCC AR6 report based on Iturbide et al. (2020) (region A), M20 (region B), Vera and Díaz (2015) (region C), Junquas et al. (2013) (region D), Gonzalez et al. (2014) (region E), and Zilli et al. (2017) (region F). The red line indicates the position of the cross section in Fig. 8.

increase could lead to a complex evolution throughout the twenty-first century, although the former seems to have a secondary impact (Mindlin et al. 2021). This makes attribution (Díaz et al. 2021) and understanding projections in SE-SA a challenge. Moreover, global climate models (GCMs) still struggle to reproduce the observed rainfall variability in the region (Vera and Díaz 2015; Díaz et al. 2021) and disagree on the sign of the future change over most of SE-SA (Fig. 1). Therefore, neither model consensus nor model performance evaluations have been able to reduce the model uncertainty.

In addition, the geographical definition of SE-SA (also extensively referred to as SESA) is diverse throughout the published literature. While in some studies the name refers to an eminently subtropical region, in others it includes the tropical region of southeastern Brazil. Figure 1a shows a set of such regions from the literature; region A is the region used in the IPCC AR6 (IPCC 2021), where the acronym is "SES." We refer to the region generally as SE-SA and use SESA and SES when appropriate, since the extent to which results are sensitive to the choice of region remains an open question, and regionalization of precipitation changes is itself a subject of our study.

Multimodel ensemble means of climate projections from the Coupled Model Intercomparison Project (CMIP) do not seem to be the best estimate for regional climate change, as when the spread among models is large and the models disagree on the sign of change, high-magnitude changes can be averaged out (Zappa et al. 2021; Hodnebrog et al. 2022). To illustrate this issue, we estimated the summer mean precipitation change between 2070 and 2099 (experiment SSP5-8.5) and 1990–2019 (historical + first 5 years of SSP5-8.5) in South America using the CMIP6 (Eyring et al. 2016) multimodel ensemble mean (MEM). Figure 1a shows the MEM precipitation change with a particular stippling, computed following Zappa et al. (2021) (see appendix A). Although the mean projected rainfall change in SE-SA is positive (Fig. 1a), uncertainties associated with both internal variability and model discrepancy in the response to forcing are large, and hence, the signal is robust at just a few grid points. Figure 1b shows the mean precipitation change projected by the MPI-ESM1-2-LR model, which depicts a robust drying change within the 10-member ensemble available. The CMIP5 version of the MPI model also showed the largest drying trends over SE-SA (Díaz et al. 2021). Moreover, there are at least three more models with drying trends in our CMIP6 ensemble, and other studies using larger ensembles found up to eight models projecting drying in SE-SA (Fig. 15 in Almazroui et al. 2021). To our knowledge, there are no previous studies exploring whether there are potential future changes in large-scale climate conditions compatible with negative rainfall trends.

Precipitation changes are driven by both thermodynamic and dynamic mechanisms. When decomposing end-of-century precipitation changes in high emission scenarios (RCP8.5) into their thermodynamic and dynamical components, dynamical terms seem to have a predominant role in explaining uncertainty in changes in mean and extreme precipitation (Pfahl et al. 2017; Elbaum et al. 2022). Circulation uncertainty is a main challenge in future climate modeling since it arises from differences between the different models' characteristics. Unlike ensemble simulations performed with the same model, projections from different models do not sample the same system (Shepherd 2014). Because of its epistemic nature, model uncertainty cannot be addressed using frequentist probabilistic analysis and requires an approach that can represent uncertainty in a conditional way.

The main objective of this study is to understand the uncertainty in projected long-term summertime rainfall changes in the SE-SA region, and we do so by addressing the following research questions:

- Are all of the plausible scenarios for the summer precipitation in SE-SA characterized by wetting conditions only? Are there plausible scenarios involving very weak wetting or even drying?
- Can variations in atmospheric circulation patterns forced by large-scale remote drivers explain the differences between contrasting SE-SA precipitation scenarios?
- How does one define a regional box for SE-SA that represents the uncertainty in large-scale circulation changes?

The article is organized as follows. Section 2a provides details on the data. The evaluation of dynamical storylines requires selecting a set of remote drivers that capture model spread in large-scale circulation, and section 2b explains how the remote drivers are selected and defined. Section 2c introduces the regression framework and section 2d explains what is meant by storyline in this article and how storylines are evaluated. To argue that the link between the remote drivers and their precipitation responses is physically coherent, section 3 shows the circulation and precipitation sensitivity to the remote drivers. The main results are presented in section 4, which shows how the responses to large-scale circulation can account for the CMIP6 ensemble spread in regional precipitation changes and provides a storyline description of the uncertainty. In addition, this section presents an explanation of how the results depend on the choice of the SE-SA region. Section 5 presents a summary and discussion of the main implications of this study.

## 2. Data and methods

### a. CMIP6 data

We use data from CMIP6 model ensembles. We employ the pattern-scaling assumption (Tebaldi and Arblaster 2014) and multiple linear regression (MLR) of circulation and precipitation responses onto indices that capture the spread in the driver responses among models (Manzini et al. 2014) as in Zappa and Shepherd (2017). We focus on the SSP5-8.5 scenario because it provides a clear forced response and compare the future climate (defined as 2070–99) in this scenario with the reference climate (1940–69) from the historical simulations. The reference period was selected in order to avoid the influence of the ozone hole on the stratospheric polar vortex.

We use data from 28 CMIP6 models (Eyring et al. 2016). We analyze sea surface temperature (tos, hereafter referred to as SST), surface temperature (tas), temperature (ta) at 250 hPa, and horizontal wind (ua, va) fields at 850 and 200 hPa. The model output (except pr) was regridded onto a T42 spatial grid using bilinear interpolation. We interpolate precipitation (pr) fields onto the same grid using conservative remapping, appropriate for fields that require flux conservation and are not smooth (Jones 1999). To assess the forced response and reduce the uncertainty due to internal variability, we compute the ensemble mean for each model by taking the average of the available ensemble members. Table 1 shows the models and the number of ensemble members per experiment.

### b. Remote drivers of large-scale circulation change in the Southern Hemisphere

#### 1) Regional and large-scale drivers

The main large-scale circulation features at subtropical and extratropical latitudes that influence variability and change in SE-SA precipitation are the midlatitude storm track and tropospheric westerlies (Berbery and Vera 1996), which are in turn influenced by the stratospheric polar vortex (Byrne and Shepherd 2018) and the Hadley cell (Saurral et al. 2017; Schmidt and Grise 2017; Nguyen et al. 2018). Part of these features' variability is captured by the main modes of variability in the SH, namely, the Southern Annular Mode (SAM) (Kidson 1988; Silvestri and Vera 2009) and the Pacific–South American (PSA) patterns, which capture an important fraction of the teleconnections in the Pacific Ocean (Mo and Higgins 1998; Mo and Paegle 2001). On the other hand, there are regional climate features that influence SE-SA, like the South American low-level jet (SALLJ) (Jones 2019; Montini et al. 2019) and the South Atlantic anticyclone (Doyle and Barros 2002; Reboita et al. 2010, 2019; Martín-Gómez et al. 2020), which can also be influenced by large-scale circulation. Large-scale drivers that have been shown to modulate the long-term forced changes in these circulation patterns are the delay in the stratospheric polar vortex breakdown date (Mindlin et al. 2021; Ceppi and Shepherd 2019), the tropical and polar amplification of global warming (Butler et al. 2010; Manzini et al. 2014; Reboita et al. 2019), and the asymmetries of sea surface temperature warming patterns (Junquas et al. 2012; Martín-Gómez et al. 2020; Lee et al. 2022). Based on the hypothesis that model uncertainty mainly originates in climate sensitivity and these very large-scale responses to forcing, in this work, we consider that the uncertainty of these latter drivers is the first source of circulation uncertainty, and hence, we call them *remote drivers*. This approach also allows building knowledge between different regions in the SH that are affected by the same remote drivers. Focusing on the remote drivers instead of regional drivers can aid the analysis of compound risk and build knowledge around storylines of global interest (McKay et al. 2023). However, there could be regional circulation responses (like the South American monsoon) that are not mediators of a large-scale circulation

TABLE 1. List of CMIP6 models used in the study. Resolutions are shown in degrees (lon × lat) or spectral truncation depending on the model. The number of ensemble members for which monthly and daily data are available is indicated for the historical and SSP5-8.5 simulations.

| | | | No. of monthly runs | | No. of daily runs | |
|---|---|---|---|---|---|---|
| | Model name | Atmospheric resolution | Historical | SSP5-8.5 | Historical | SSP5-8.5 |
| 1 | ACCESS-CM2 | 1.258 × 1.8758 | 3 | 1 | 1 | 1 |
| 2 | ACCESS-ESM1-5 | 1.25 × 1.875 | 10 | 3 | 10 | 3 |
| 3 | BCC-CSM2-MR | T106 | 3 | 1 | 3 | 1 |
| 4 | CAMS-CSM1-0 | T106 | 2 | 2 | 2 | 2 |
| 5 | CanESM5 | T63L49 | 25 | 25 | 25 | 10 |
| 6 | CESM2 | 0.9 × 1.25 | 11 | 2 | 11 | 3 |
| 7 | CESM2-WACCM | 0.9 × 1.25 | 3 | 3 | 3 | 3 |
| 8 | CMCC-CM2-SR5 | 1 × 1 | 1 | 1 | 1 | 1 |
| 9 | CNRM-CM6-1 | T127 | 30 | 6 | 30 | 6 |
| 10 | CNRM-ESM2-1 | T127 | 10 | 5 | 10 | 5 |
| 11 | EC-Earth3 | TL255 | 1 | 1 | 1 | 1 |
| 12 | FGOALS-g3 | 0.9 × 1.25 | 6 | 4 | 6 | 4 |
| 13 | HadGEM3-GC31-LL | N96 | 4 | 4 | 4 | 4 |
| 14 | HadGEM3-GC31-MM | N216 | 4 | 4 | 4 | 1 |
| 15 | IITM-ESM | T62L64 | 1 | 5 | 1 | 1 |
| 16 | INM-CM4-8 | 2 × 1.5 | 1 | 1 | 3 | 1 |
| 17 | INM-CM5-0 | 2 × 1.5 | 10 | 1 | 10 | 1 |
| 18 | KACE-1-0-G | N96 | 3 | 3 | 3 | 3 |
| 19 | MIROC6 | T85 | 50 | – | 10 | 3 |
| 20 | MIROC-ES2L | T42 | 10 | 2 | 10 | 1 |
| 21 | MPI-ESM1-2-HR | T127 | 10 | 10 | 10 | 1 |
| 22 | MPI-ESM1-2-LR | T63 | 10 | 10 | 10 | 10 |
| 23 | MRI-ESM2-0 | TL159 | 5 | 1 | 5 | 1 |
| 24 | NESM3 | T63 | 5 | 2 | 5 | 2 |
| 25 | NorESM2-LM | 2 × 2 | 3 | 1 | 3 | 1 |
| 26 | NorESM2-MM | 1 × 1 | 3 | 1 | 2 | 1 |
| 27 | TaiESM1 | 0.9 × 1.25 | 1 | 1 | 1 | 1 |
| 28 | UKESM1-0-LL | N96 | 7 | 2 | 5 | 2 |

response. Considering how these remote drivers project onto regional circulation features such as the SALLJ or the Hadley cell (as M20 did with the Southern Annular Mode) and evaluating if there are regional sources of uncertainty (such as the South American monsoon) that are independent of large-scale drivers is beyond the scope of this study and could be a good follow-up of this work.

Figure 2 summarizes dynamical mechanisms associated with remote driver (RD) responses explaining summer rainfall trends in SE-SA, either observed or projected. In this section, we explain the rationale behind the RDs considered and the definition of indices that capture their response.

### 2) LARGE-SCALE REMOTE DRIVERS

M20 showed that future changes in the SAM can be explained by the effect of two large-scale remote drivers, namely, the tropical upper-troposphere warming ($\Delta T_{trop}$) and extension of the springtime stratospheric polar vortex circulation into the summer (represented through the delayed vortex breakdown date, ΔVB). The tropospheric circulation response of both projects onto changes in the SAM, although they have qualitatively different effects on circulation. Note that $\Delta T_{trop}$ contributes by strengthening the SH westerly winds and ΔVB contributes with a hemispheric poleward shift of the westerly winds in summer (Ceppi and Shepherd 2019). Therefore, although both project on the SAM change, their circulation and therefore precipitation responses were found to be opposite in sign and it is therefore more appropriate to treat them separately. The term $\Delta T_{trop}$ can induce expansion of the Hadley cell (e.g., Schmidt and Grise 2017; Butler et al. 2010) and a drying response in SE-SA (Junquas et al. 2013; Gonzalez et al. 2014; M20). The poleward shift in the westerlies driven by ΔVB enhances easterly anomalies between 30° and 45°S over the eastern coast of South America, which lead to more storms from the Atlantic to the coast of SE-SA, increasing precipitation (Wu and Polvani 2015; M20).

Dynamical changes forced by ozone depletion have been proposed as drivers of the observed summer rainfall trends between 1960 and 1999 (Gonzalez et al. 2014). However, Mindlin et al. (2021) recently showed that the role of ozone does not appear to be as important for precipitation trends in SE-SA when it is studied in combination with the effect of the mean trends, $\Delta T_{trop}$ and ΔVB. We therefore only focus on the influence of GHGs on the stratosphere and use 1940–69 as the reference period, which avoids capturing the influence of the ozone hole in the ΔVB index.

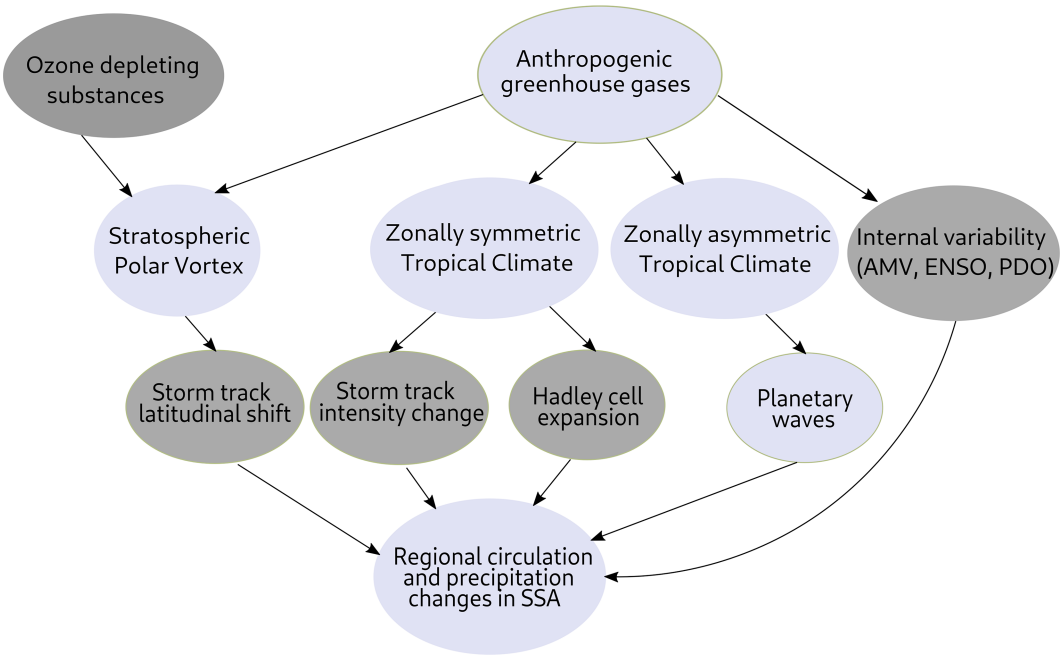


FIG. 2. Schematic for the remote driver analysis. In order from top to bottom, the rows show anthropogenic forcings, large-scale phenomena outside the midlatitude troposphere, tropospheric dynamical phenomena, and regional changes. The blue shading indicates the elements explicitly considered in this study. In this article, we quantify changes in "zonally symmetric tropical climate" and "zonal asymmetries in tropical climate" with the $\Delta T_{\text{trop}}$ index and the two Pacific Ocean ASYM-SST indices defined in section 2b, respectively. However, other indices could be explored. For example, an ITCZ index could be added for the former and an Indian Ocean SST index for the latter.

M20 showed that these two remote drivers captured a significant fraction of the model spread in regional precipitation and represented the uncertainty with four dynamical storylines. However, none of the identified storylines in M20 could explain a drying change for summer in SE-SA. In this work, we expand the set of RDs in M20 and include asymmetric sea surface temperature (ASYM-SST) warming patterns. The main motivation for the selection of this additional remote driver is that it has been identified in previous works as a relevant RD mediating the precipitation response in SE-SA to global warming via planetary wave teleconnections (Junquas et al. 2012). Moreover, the SST warming patterns simulated by GCMs show a large spread across the CMIP6 ensemble (e.g., Yang et al. 2021; Lee et al. 2021), representing one of the most puzzling features of near-term climate change responses (Lee et al. 2022). Hence, they are good RD candidates for the regional response. Figure 3 shows the CMIP6 ensemble mean and spread of the total (Figs. 3a,d), zonally symmetric (Figs. 3b,e), and zonally asymmetric (Figs. 3c,f) SST change in the tropical Pacific scaled by the global mean warming in each model. The MEM change in the mean state of SSTs presents a "Niño-like pattern" characterized by a reduction of the east–west SST gradient (Fig. 3c), but there is a large spread in the spatial pattern of the response (Fig. 3f). A positive change in ASYM-SST stands out to the east of New Zealand (Fig. 3c); however, there is no model spread there. The spread is found in the central and eastern tropical Pacific and the subtropical east Pacific; the latter is positively correlated with the central Pacific spread.

#### 3) INDEX DEFINITION

To evaluate the response to ΔVB and $\Delta T_{\text{trop}}$, we follow M20. There is no consensus on an index that captures the spread in ASYM-SST changes (Lee et al. 2021). We therefore define two indices based on the two independent regions where the standard deviation between models is maximum in the tropical ASYM-SSTs (CP and EP in Fig. 3). Since previous studies assessed precipitation change uncertainty using other indices that capture similar responses (e.g., Yang et al. 2021), we make our results comparable by showing the correlations between our indices and other ENSO-related indices (Table 2).

In summary, we evaluate the remote driver responses with the following indices:

- Temperature change at 250 hPa averaged between 15°S and 15°N ($\Delta T_{\text{trop}}$)
- Change in the climatological vortex breakdown date in Julian days (ΔVB)
- Central Pacific ASYM-SST change averaged over the box [5°N–5°S, 180°E–110°W] ($\Delta \text{CP}_{\text{asym}}$)
- Eastern Pacific ASYM-SST change averaged over the box [0°N–10°S, 100°–80°W] ($\Delta \text{EP}_{\text{asym}}$)

The vortex breakdown date is defined as the time when zonal mean zonal winds at 50 hPa first weaken below 19 m $s^{-1}$

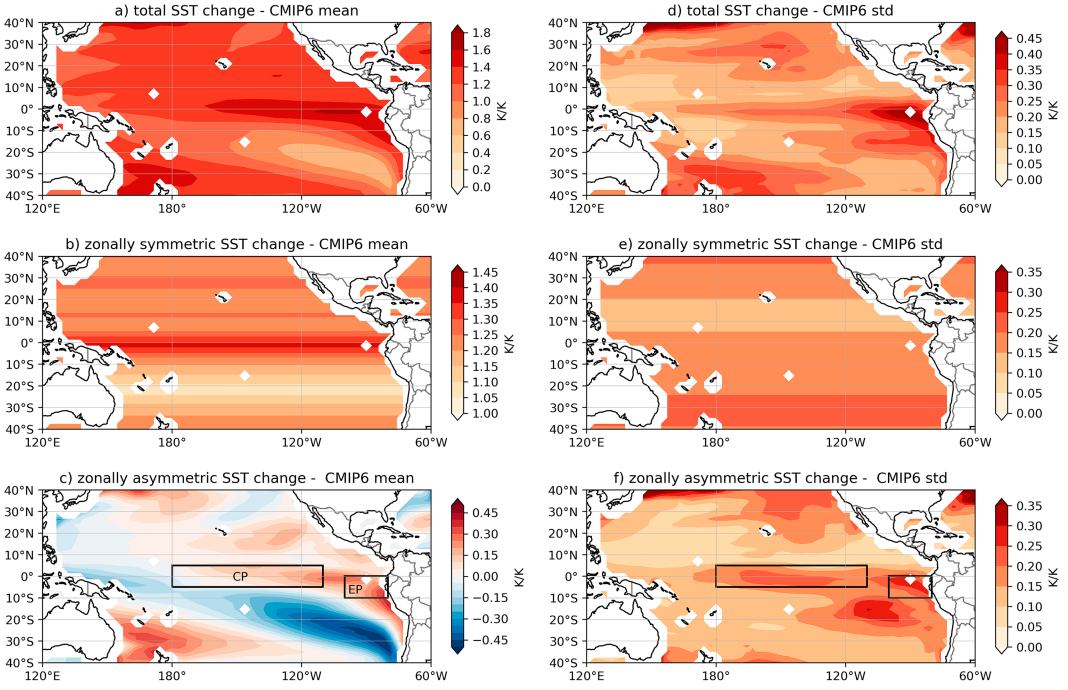


FIG. 3. (a) Summer sea surface temperature (SST) change by the end of the century (2070–99) with respect to the reference period (1940–69) scaled by the global mean surface temperature change over the same period ($\Delta T$) projected by the CMIP6 models forced with the SSP5-8.5 scenario (models listed in Table 1). (b) Zonal mean SST change per degree of $\Delta T$. (c) Asymmetric SST change per degree of $\Delta T$, computed as the difference between (a) and (b). (d)–(f) One standard deviation of the ensemble for the fields in (a)–(c), respectively.

in their seasonal march (Mindlin et al. 2021). ASYM-SST is defined as the difference between the total SST change and the zonally averaged SST change across the Pacific basin. The terms $\Delta T_{\text{trop}}$, $\Delta\text{CP}_{\text{asym}}$, and $\Delta\text{CP}_{\text{asym}}$ are in kelvins.

### c. *Multiple linear regression framework*

An MLR is built to predict the models' response in a field $\Delta C_{xm}$ (where $m$ is the model and $x$ is the grid point) scaled by the global warming level, $\Delta P_{xm} = \Delta C_{xm}/\Delta T_m$, to the independent variables. The independent variables are the standardized RD indices defined in section 2b after scaling by global warming (GW):

$$\Delta P_{xm} = a_x + b_x\left(\frac{\Delta T_{\text{trop}}}{\Delta T}\right)'_m + c_x\left(\frac{\Delta \text{VB}}{\Delta T}\right)'_m + d_x\left(\frac{\Delta \text{CP}_{\text{asym}}}{\Delta T}\right)'_m + e_x\left(\frac{\Delta \text{EP}_{\text{asym}}}{\Delta T}\right)'_m + \epsilon_{xm}. \quad (1)$$

The prime indicates a standardized anomaly. The term $a_x$ is the MEM response per degree of global warming. The coefficients $b_x$, $c_x$, $d_x$, and $e_x$ quantify the sensitivity to one standard deviation in tropical warming, TW = $(\Delta T_{\text{trop}}/\Delta T)_m$; vortex breakdown delay, $\text{VB}_{\text{delay}} = (\Delta\text{VB}/\Delta T)_m$; and CP and EP warmings, CP = $(\Delta\text{CP}_{\text{asym}}/\Delta T)_m$ and EP = $(\Delta\text{EP}_{\text{asym}}/\Delta T)_m$. Their estimated values $\hat{a}_x$, $\hat{b}_x$, $\hat{c}_x$, $\hat{d}_x$, and $\hat{e}_x$ are computed

TABLE 2. Pearson correlation coefficients between tropical SST remote driver indices used in this work and classical indices used to characterize tropical Pacific SST anomalies, before and after scaling by global-mean warming (see section 2c for definitions). Correlations with the tropical upper-tropospheric warming index (TW) are included for completeness. Bold font values indicate significant correlations at the 99% level according to a two-tailed $t$ test.

| | Niño-4 | Niño-3.4 | Niño-3 | Niño-1 + 2 | Zonal gradient | Zonal mean | CP | EP | TW |
|---|---|---|---|---|---|---|---|---|---|
| Before scaling by GW | | | | | | | | | |
| CP | 0.33 | **0.41** | 0.21 | 0.07 | −0.32 | −0.11 | **1** | 0.00 | 0.15 |
| EP | −0.07 | 0.06 | 0.23 | **0.55** | **−0.56** | **0.95** | 0.00 | **1** | −0.11 |
| After scaling by GW | | | | | | | | | |
| CP | **0.53** | **0.67** | 0.17 | −0.16 | **−0.33** | −0.13 | **1** | 0.00 | 0.13 |
| EP | 0.06 | 0.27 | **0.69** | **0.9** | **−0.5** | **0.97** | 0.09 | **1** | 0.19 |

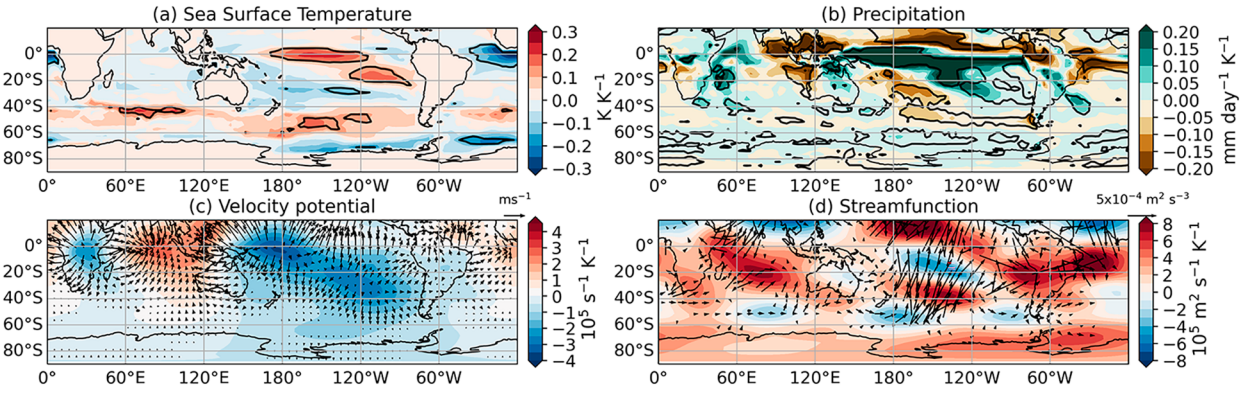


FIG. 4. (a) Sensitivity of SST per degree of $\Delta T$ associated with one standard deviation positive change in CP warming ($\Delta CP_{asym}/\Delta T$) evaluated with the MLR model in section 2. (b)–(d) As in (a), but for precipitation (pr), velocity potential (shading) and divergent wind (arrows) at 200 hPa, and streamfunction (shading) and wave activity flux (arrows) at 200 hPa, respectively. See text for details. Contours indicate areas with regression coefficients statistically significant at the 90% level, evaluated with a two-tailed $t$ test, and then applying a 20% false discovery rate global test.

by fitting the model [(1)] to the CMIP6 data using ordinary MLR. The term $\epsilon_{xm}$ is the residual from the regression. Statistical significance for the MLR is tested with an $F$ test at the 90% confidence level and a two-tailed Student's $t$ test at the 90% confidence level for the regression coefficients. We also apply a 20% false discovery rate test to global maps (Wilks 2016; Cortés et al. 2020). Applying an MLR model implies assuming independent and identically distributed residuals, which is not expected to be the case for CMIP data (Knutti et al. 2013). Therefore, we apply a leave-one-out cross-validation to ensure that the results are not artifacts of shared model biases or strong outliers (not shown).

### d. *Storyline framework*

In this work, a storyline is defined as the climate change associated with a combination of RD responses to anthropogenic forcing within an empirical distribution of responses. We call this distribution of RD responses plausible because it is estimated from the output of experiments run with an ensemble of CMIP models, which are meant to represent the physical response to anthropogenic forcing. A way of presenting a storyline description of regional uncertainty is by comparing the regional climate responses associated with a small set of representative storylines. Zappa and Shepherd (2017) first described a set of storylines for Mediterranean regional changes by selecting four combinations of two RD responses equally distant from the multimodel ensemble mean response, a way of sampling the RD distribution. The same was done in M20. In this study, instead of presenting a set of storylines and comparing them, we particularly focus on finding the extreme wet and dry storylines. For this, we produce an ensemble of $10^6$ storylines by sampling the RD distribution, and then we subsample the extreme wet and dry storylines and find the combination of RD responses that lead to these two storylines. We use this framework in section 4 and explain the calculation details in appendix B.

## 3. Atmospheric circulation and precipitation sensitivity to remote drivers

### a. *Zonally symmetric remote drivers: Tropical warming and stratospheric polar vortex*

To understand how the circulation changes associated with TW and $VB_{delay}$ can explain the precipitation changes, M20 analyzed the extratropical circulation response to TW and $VB_{delay}$ in terms of both u850 and storm density. Here, we repeat the analysis with u850 (Fig. S1 in the online supplemental material) and confirm that the two responses show a fairly zonally symmetric response and remarkable similarity with the structures found by applying the same framework (though without also regressing onto CP and EP) to an ensemble of CMIP5 models (Fig. 5 in M20). Given that this circulation response was extensively analyzed in M20, we refer the interested reader to M20. In this article, we focus on analyzing the circulation response to the asymmetric remote drivers (CP and EP).

### b. *Asymmetric remote drivers: Sea surface temperature patterns*

In this subsection, we characterize the influence of ASYM-SST patterns in the CMIP6 model ensemble on circulation and pr changes.

We apply the MLR from section 2c to changes in SSTs, pr, and the zonal and meridional components of lower-level (850 hPa) and upper-level (200 hPa) winds (u850 and u200, v200).

Figures 4a and 4b show the SST and pr sensitivity to CP warming and Figs. 5a and 5b show the same for EP warming. In the tropics and over the region of the box used to define the index, the SST sensitivity to the CP index shows a warming of 0.3 K $K^{-1}$. In addition, it captures a similar warming in the eastern subtropics. The spread in these two regions is positively correlated (section 2b), which explains why the index well captures the SST warming in both regions (Fig. 3). Investigating the cause of this correlation is beyond the scope of this article. The pr sensitivity shows a signal over the tropical

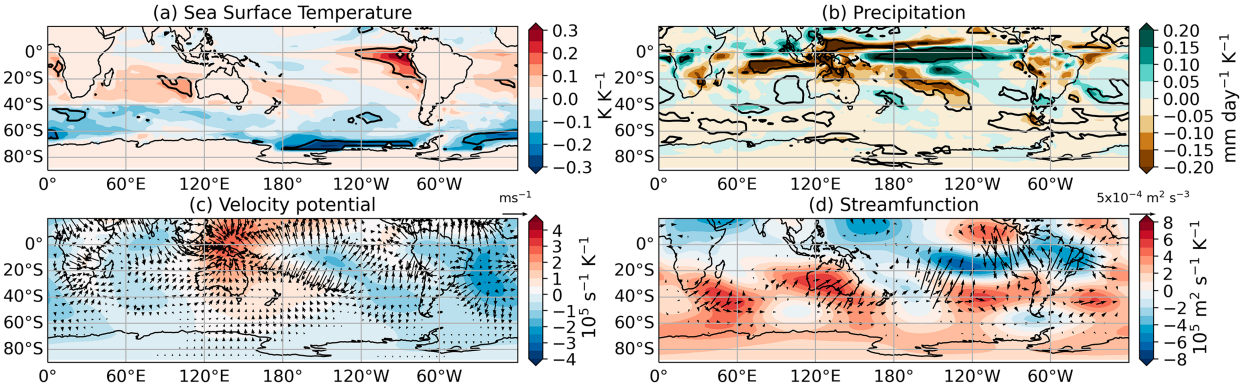


FIG. 5. As in Fig. 4, but for responses associated with one standard deviation positive change in EP warming ($\Delta EP_{asym}/\Delta T$).

Pacific, coherently positioned to the west of the SST anomaly. The same is observed in the subtropical central Pacific (Fig. 4b). The SST sensitivity to the EP warming (Fig. 5a) shows a warming of 0.4 K $K^{-1}$ in the region where the index is defined and a cooling signal in the extratropics, collocated with the low-level wind forcing (u850; Fig. S1d).

We study the tropical and extratropical circulation responses, discriminating between the divergent and rotational responses. Figures 4c and 4d show velocity potential and streamfunction, respectively, for CP warming; Figs. 5c and 5d show the same but for EP warming. We overlay the divergent winds with the velocity potential and horizontal wave activity fluxes (WAF) with the streamfunction. The WAF are diagnosed using the method described in Takaya and Nakamura (2001). Upper-level divergence serves as a diagnostic for convection, whereas the WAF diagnostic has been extensively used to identify wave sources or sinks associated with large-scale phenomena, as well as teleconnection pathways. In this case, the regression pattern of (u200, v200) is analyzed as the anomaly or snapshot, and the MEM climatological wind field in the future period (2070–99) is the mean basic flow. Regions of WAF divergence are regions where enhanced WAF can be associated with tropical Pacific warming (either CP or EP), whereas the convergence of WAF indicates regions that can be reached and dynamically affected by this RD.

In response to CP warming, the velocity potential shows upper-level wind divergence and positive pr changes over the west tropical and central subtropical portions of the Pacific (Fig. 4c). On the other hand, the velocity potential and the associated upper-level wind convergence maximize over the eastern Indian Ocean (Fig. 4c), in association with descending motion and negative pr changes (Fig. 4b). In Fig. 4d, we see the characteristic pair of upper-level anticyclonic anomalies poleward of the SST anomaly in both hemispheres and a wave train extending from the central equatorial Pacific Ocean to the Atlantic Ocean. The wave train induces an anticyclonic anomaly over the southern tip of South America and a cyclonic anomaly over SE-SA, favoring moisture convergence as has been extensively described in the literature (e.g., Grimm et al. 2000; Junquas et al. 2013). Spatial wavenumber analysis (not shown) shows that most of the circulation response projects onto wavenumber 1 in the tropics, wavenumber 2 in the subtropics, and wavenumber 4 in the extratropics.

The velocity potential response to EP warming shows a maximum over the Maritime Continent, associated with strong upper-level wind convergence, descending motion, and large negative pr changes (Figs. 5b,c). On the other hand, the response over the central South Pacific Ocean is a northwest to southeast elongated velocity potential minimum with two associated divergence regions (Fig. 5c). The tropical divergence region is associated with positive pr changes (Fig. 5b). WAF emanating both from the western South Pacific Ocean (55°S, 150°W) and from the tropical Pacific SST anomaly reach South America (Fig. 5d). Another Rossby wave train–like pattern extends over the eastern Pacific Ocean, meridionally constrained to the west coast of South America (Fig. 5d). It induces an anticyclonic anomaly over the tip of South America, although weaker and westward compared to that induced by CP warming. EP warming also induces cyclonic anomalies over SE-SA, although the anomaly center is located farther south compared to that induced by CP warming. Spatial wavenumber analysis (not shown) shows most of the response projecting onto wavenumber 1 in the tropics and subpolar regions (around 60°S), wavenumber 2 in the extratropics (over 40°S) and subpolar regions (around 60°S), and wavenumber 4 in the subtropics (over 20°S) and extratropics (over 40°S).

### c. *Precipitation sensitivity to remote drivers*

Figure 6 shows the pr sensitivity in South America to one standard deviation in each RD index. As found in M20, we see that TW contributes to drying in most of the domain, but in particular over the extratropics. This has been explained by a subsidence anomaly due to shifts in the Hadley cell (e.g., Junquas et al. 2013; Saurral et al. 2017). Consistent with this, a decrease of cyclone density north of 40°S has also been identified in response to TW (see also u850 in Fig. S1 and M20). On the other hand, $VB_{delay}$ and CP warming contribute to a large drying in the tropics and a positive pr change in SE-SA and particularly in southeastern Brazil, in association with an increased cyclone density (M20). The structure of the wetting

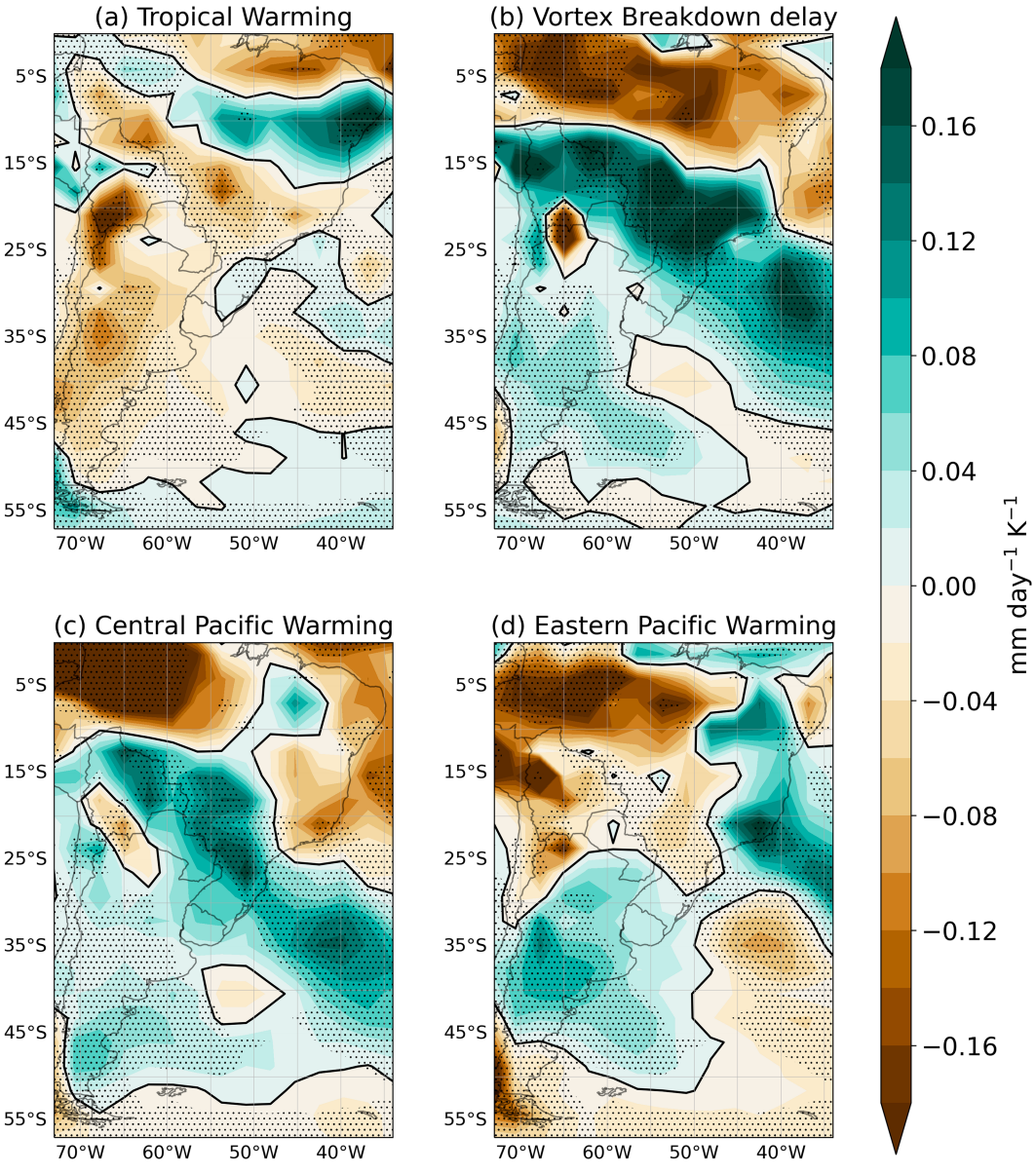


FIG. 6. (a) Sensitivity of pr per degree of $\Delta T$ associated with one standard deviation positive change in TW warming ($\Delta T_{trop}/\Delta T$). (b)–(d) As in (a), but in response to $VB_{delay}$ ($\Delta VB/\Delta T$), CP warming ($\Delta CP_{asym}/\Delta T$), and EP warming ($\Delta EP_{asym}/\Delta T$), respectively. Stippling indicates areas where the regression is statistically significant at the 90% level, evaluated with an $F$ test, and then applying a false discovery rate global test at the 20% level.

signal resembles a poleward shift of the South Atlantic convergence zone, a feature described in the last decades (Zilli et al. 2019); we see the same feature farther south in response to CP warming.

Overall, the cyclonic anomalies induced by CP and EP warming (Figs. 4d and 5d) lead to wetting over a large part of South America. However, the cyclonic circulation response to CP warming has a large extent, covering most of the continent, while the cyclonic response to EP is constrained to the center of Argentina, which makes the pr change patterns locally dissimilar.

## 4. Storyline representation of summer precipitation changes in SE-SA

We now analyze how the regional pr responses to RDs can jointly explain plausible future drying or large wetting conditions in SE-SA. We first evaluate the MLR performance by estimating the GCM responses from linear combinations of their RD response for each model, referred to as "reconstructed" responses (RRs) to RD. The median absolute deviation (MAD) of the RR is shown in Table 3. To analyze the total spread that the storylines can represent, we emulate $10^6$ samples from the

TABLE 3. For each box in Fig. 1, the combination of storyline indices (one per remote driver) that result in the mean extreme wet and dry storylines (rows 3–6) (see section 4b) and the corresponding Δpr (mm day$^{-1}$ K$^{-1}$) (row 7). For each region, the median absolute deviation (MAD) of the reconstructed model pr responses after averaging over the regions is shown. The models are referenced with their corresponding number in Table 1, where an asterisk (*) means that the model is not exactly in the corresponding storyline quadrant, but three of the four remote drivers coincide with the corresponding storyline quadrant.

| | Region A | | Region B | | Region C | | Region D | | Region E | | Region F | |
|---|---|---|---|---|---|---|---|---|---|---|---|---|
| | Wet | Dry | Wet | Dry | Wet | Dry | Wet | Dry | Wet | Dry | Wet | Dry |
| TW | −0.76 | 0.96 | −1.65 | 1.80 | −1.91 | 1.80 | −0.55 | 0.68 | −1.19 | 1.34 | −0.1 | 0.52 |
| $VB_{delay}$ | 1.58 | −1.18 | 0.68 | −0.44 | 0.69 | −0.55 | 1.39 | −1.22 | 1.92 | −1.70 | 2.38 | −2.07 |
| CP | 1.00 | −0.8 | 0.69 | −0.34 | 0.15 | −0.19 | 2.04 | −2.15 | 1.49 | −1.52 | −0.52 | 0.98 |
| EP | 1.68 | −1.73 | 1.83 | −1.90 | 1.80 | −1.91 | 0.84 | −0.15 | 0.46 | −0.05 | 1.02 | −0.88 |
| Δpr | 0.19 | −0.15 | 0.34 | −0.12 | 0.38 | −0.10 | 0.41 | −0.10 | 0.30 | −0.09 | 0.57 | −0.35 |
| Model(s) | 12*, 26* | 9, 22, 23 | 12*, 26* | 9, 22, 23 | 12*, 26* | 9, 22, 23 | 12*, 26* | 9, 22, 23 | 12*, 26* | 9, 22, 23 | 12, 26 | 3, 8, 20 |
| MAD | 0.40 | | 0.07 | | 0.04 | | 0.05 | | 0.08 | | 0.15 | |

remote driver distribution (Fig. 7; see appendix B for calculation details). We refer to these as "emulated" storylines (SL).

Figure 8a shows the pr response of the MEM and to each RD along the red line depicted in Fig. 1a, a cross section through the SE-SA region from southwest to northeast. The MEM shows a wetting response over the entire region. The responses to the RDs locally reach the same magnitude as the MEM. Figure 8b shows the pr response along the cross section from each individual GCM (gray lines) and the spread explained by the SL (colored shading). In the sector including regions B and C and the southwest part of regions D and E, the MEM response is about 0.12 mm day$^{-1}$ K$^{-1}$ and TW drives the largest drying signal (−0.07 mm day$^{-1}$ K$^{-1}$), while the remaining remote drivers have a wetting signal ($VB_{delay}$, 0.03 mm day$^{-1}$ K$^{-1}$; CP, 0.02 mm day$^{-1}$ K$^{-1}$; and EP, 0.07 mm day$^{-1}$ K$^{-1}$). Between 27°S, 54°W and 23°S, 47°W, a sector that includes the northeastern part of regions D and E, the responses to CP warming and $VB_{delay}$ (0.10 and 0.15 mm day$^{-1}$ K$^{-1}$) exceed the MEM change (0.09 mm day$^{-1}$ K$^{-1}$) and some models show drying changes of the same magnitude as the MEM (Fig. 8b). On the other hand, the northernmost sector, which covers part of region F, shows the largest spread. Here, all the RDs have a strong influence. In particular, EP warming and $VB_{delay}$ drive a large positive signal (0.12 and 0.13 mm day$^{-1}$ K$^{-1}$), while CP warming (−0.09 mm day$^{-1}$ K$^{-1}$) and TW (−0.05 mm day$^{-1}$ K$^{-1}$) drive negative and smaller changes, yet still significant compared to the MEM (0.10 mm day$^{-1}$ K$^{-1}$).

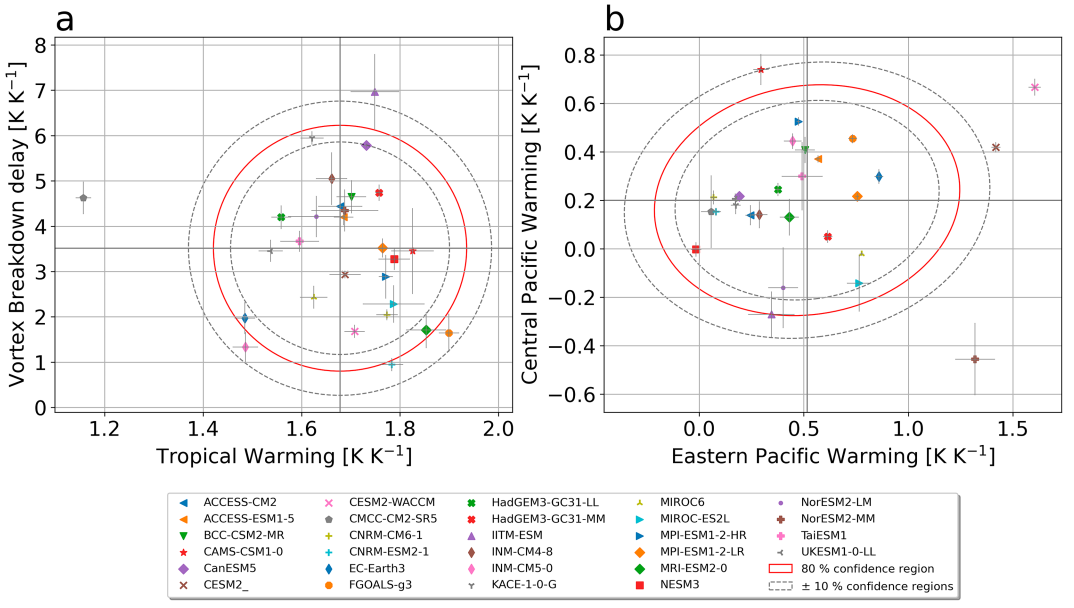


FIG. 7. CMIP6 model responses in (a) $VB_{delay}$ and TW, and in (b) CP and EP. The red ellipse shows the 80% confidence region of the joint $\chi^2$ distribution with four degrees of freedom; the dashed ellipses show the 70% and 90% confidence regions. Error bars show the 95% confidence interval in the individual model responses for the remote driver indices. The confidence intervals are estimated from the year-to-year variability assuming white noise in the remote drivers and accounting for the number of ensemble members available for each model as in M20.

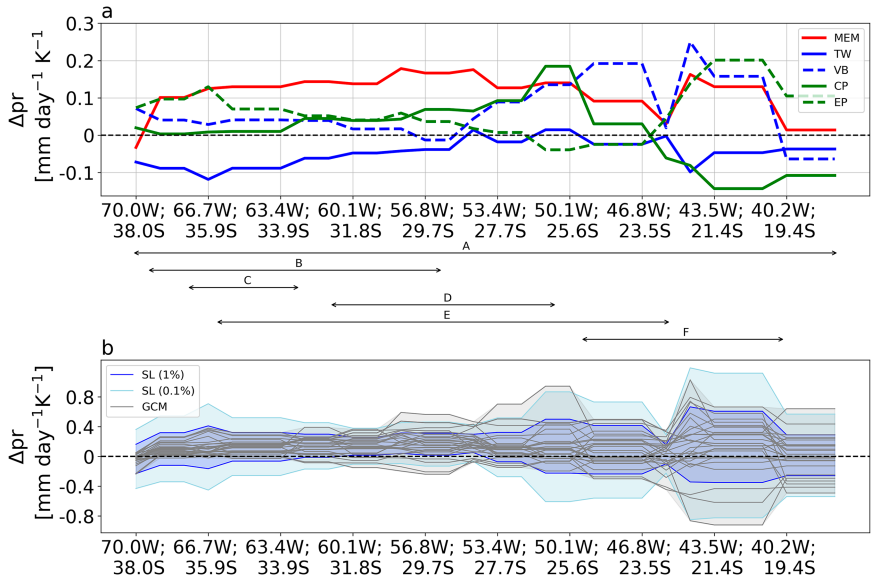


FIG. 8. (a) Cross section of sensitivity coefficients ($\hat{a}_x$, $\hat{b}_x$, $\hat{c}_x$, $\hat{d}_x$, $\hat{e}_x$) from the MLR applied to pr along the red line in Fig. 1a. (b) In gray, pr responses in each individual model of the CMIP6 ensemble. In blue (light blue), 99% (99.9%) pr change range of the storylines from the emulated storyline ensemble evaluated as explained in section 2d and appendix B. Note the different vertical scale between the two panels. The correspondence of the cross section with the different regions shown in Fig. 1a (A–F) is indicated with the horizontal double-headed arrows.

The extent to which the combination of RD responses can explain extreme wet and dry changes is shown by selecting the most extreme 0.5% and 0.05% of the SL for each box, which represent the lowest and highest 99th and 99.9th percentile of the changes (Fig. 8b). The SL explain the spread of the CMIP6 responses to a large extent; however, between 38°S, 70°W and 30°S, 57°W, the extreme range (99.9% quantile) of storylines overestimates the model spread and may be interpreted as unexplored values of the plausible distribution (Fig. 8b). Furthermore, over the central-east and northeastern sectors, the 99% quantile does not capture the model spread, while the 99.9% quantile does. This suggests that in these sectors, the CMIP6 ensemble is sampling some of the more extreme storylines (Fig. 7).

### *a. Consequences of regional aggregation*

Regional aggregation or averaging over a spatial box is used in climate science to quantify responses over a region and to communicate plausible projections. For example, Iturbide et al. (2020) recently updated the IPCC climate reference regions for subcontinental analysis. Figure 1a includes a selection of boxes considered in the literature to analyze pr changes from the subtropics to the tropics of south and eastern South America. They were all used for different purposes, hence the different domain definitions. Box A is the one defined in the IPCC WGI report (IPCC 2021) as the "Southeastern South America (SES)" region (Iturbide et al. 2020). Box B was used by M20 to study the sensitivity of summer rainfall projections in SE-SA to extratropical remote drivers. Box C was used by Vera and Díaz (2015) to assess observed trend biases in CMIP5 models. Junquas et al. (2013) used box D to focus on tropical influences on rainfall changes in subtropical SE-SA. Gonzalez et al. (2014) used box E to investigate the role of ozone depletion in driving observed trends in SE-SA. Box F is the study region used by Zilli et al. (2017), who analyzed future projections over the south of Brazil.

To illustrate the effect of regional aggregation, in Fig. 9, we show the individual models' precipitation response and the reconstructed response averaged over the boxes in Fig. 1a against each of the RDs. When averaged over box A, the changes are very small and the MLR shows little explanatory power (Figs. 9a–d). This is because an average over box A represents an average over drying and wetting subregions (Figs. 6 and 8). However, when considering subregions of box A, the spread between the changes becomes explainable in terms of the large-scale drivers. Figures 9e–h, 9i–l, 9m–p, 9q–t, and 9u–x show boxes B, C, D, E, and F, respectively. In particular, TW can explain the model spread particularly well in boxes B, C, and E, whereas $\mathrm{VB}_{\mathrm{delay}}$ can explain the model spread in boxes E and F. On the other hand, CP warming can explain the model spread in region D and also shows some explanatory power over regions E and F, whereas EP warming can explain the spread in regions B and C and to a lesser extent in regions D and F. This explains why dynamical storylines might not be useful over box A, while in smaller regions they can be fit for purpose when representing uncertainty. This is not the first example of how aggregation can lead to misleading results: Breul et al. (2023) recently showed that this is the case for the emergent constraint on the SH wintertime zonal-mean jet response to global warming, which could

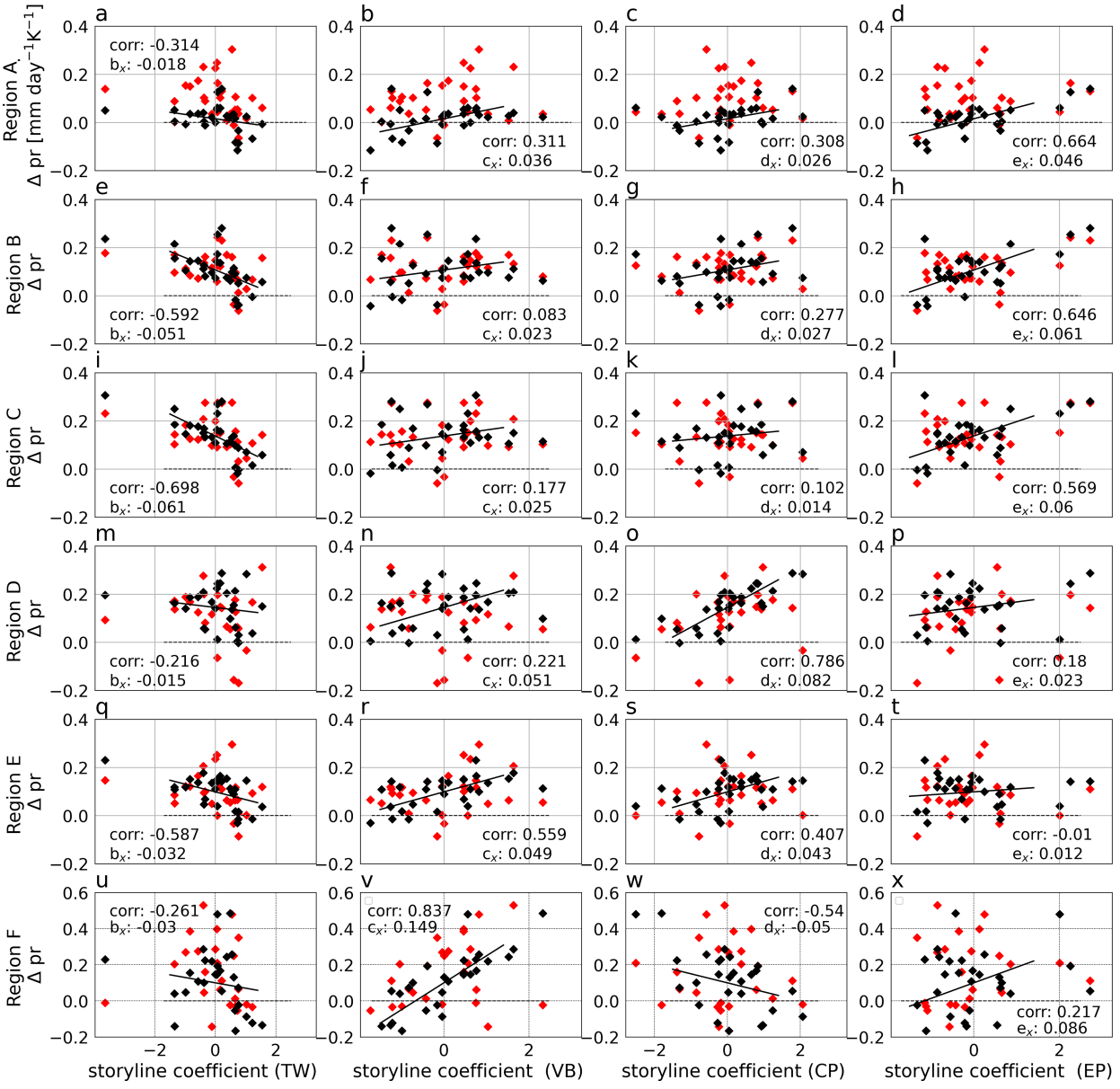


FIG. 9. Scatterplots show the individual model responses (GCM; black) and reconstructed model responses (RR; red; evaluated following the framework in section 2c) against the standardized remote driver indices. The pr values are shown in units of mm day$^{-1}$ K$^{-1}$. The regression coefficients (mm day$^{-1}$ K$^{-1}$) from the MLR model averaged over each region and the Pearson correlation coefficient between each model's RD response and the pr change averaged over the box are also shown in each panel. Note the different vertical scale for region F.

be better addressed with regional metrics rather than with the zonal mean.

As mentioned in section 1, in this work, we want to understand the ensemble spread in the SE-SA precipitation by considering the combined influence of previously identified remote drivers (Fig. 2). Figure 10a shows the spread of the pr changes in the CMIP6 ensemble, the reconstructed responses (RR), and the spread of the emulated storylines (SL; see appendix B and Fig. 8). In box A, the large-scale drivers have little explanatory power and the RR cannot reproduce the spread or the median aggregated precipitation response (Fig. 10a). When considering boxes B–E, we find there is an overall agreement in the median response (0.5 ± 0.1 mm day$^{-1}$) and the interquartile range (Fig. 10a). Meanwhile, the response is very different for box F, which comprises a tropical region where the influence of the considered large-scale drivers is different and interannual summer precipitation variability is driven by other mechanisms like the South American monsoon. Moreover, the SL are able to well reproduce the median and the full range of responses, although they fail to capture the largest drying changes. Figure 10b shows the same as Fig. 10a but considering pattern scaling, that is, showing the results per degree of

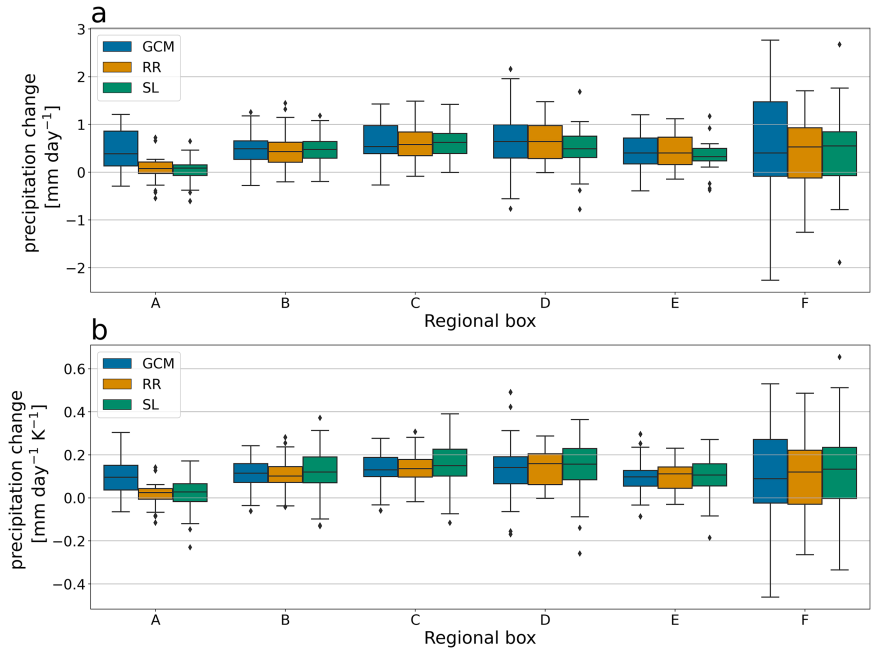


FIG. 10. Pr changes averaged over the regional boxes in Fig. 1, showing (a) the total responses (mm day$^{-1}$) and (b) the precipitation change per degree of warming (mm day$^{-1}$ K$^{-1}$). Blue boxplots show the pr change in the CMIP6 ensemble (GCM), yellow boxplots show the pr change in the same CMIP6 ensemble reconstructed with the sensitivities to the remote drivers evaluated with the regression model (RR), and green boxplots show the pr change of the full storyline ensemble evaluated as described in section 2d and appendix B (SL).

warming. The agreement in the median and full range of the responses is even better when the responses are scaled by the level of global warming (Fig. 10b). We find a similar behavior of the modeled and emulated spreads, meaning that the pattern-scaling assumption is good for the purpose of this study. Moreover, the spread explained here captures the uncertainty associated with large-scale circulation and not climate sensitivity.

### b. *Extreme storylines assessment*

To evaluate the extreme storylines and associated RDs, we average the pr change of each emulated storyline (SL) over each box and sample the 99% quantile (0.5% driest and 0.5% wettest) of the SL ensemble. We identified the mean of the RD responses for each quantile for each box separately. The combination of remote driver responses and associated pr change is shown in Table 3 for each box. We find that the extreme wetting and drying storylines averaged over boxes A, B, C, D, and E result from the same combination of signs in the RD responses, whereas the extreme storylines for region F result from a different RD combination. In Fig. 11, we show the remote driver responses associated with the extreme storylines for box B (Figs. 11a,b) and box F (Figs. 11c,d). Box B is the largest region (from B, C, D, and E) that does not overlap with region F. A larger box is preferred over a small one as it is more likely representative of the whole region. The blue and red dots in Fig. 11 represent the wettest storylines and driest storylines, respectively. The storylines fall within the 80% confidence region of the quantile function of the chi-squared distribution with four degrees of freedom (red ellipse); therefore, what we define as extreme lies within the confidence region that has been considered extreme yet plausible in previous studies (Zappa and Shepherd 2017; M20). Although the driest and wettest quadrant could have been inferred from the signs of the remote driver responses, this quantitative analysis determines which of the RDs is most relevant for each regional box (Table 3).

The nuanced ways in which remote drivers can influence pr patterns in South America lead to a variety of trends, as shown in Fig. 9. In box B, the wetting response is associated with positive CP and EP warmings, and therefore, the extreme precipitation trends will occur when these RDs jointly act in a warming direction. However, given that CP warming drives a drying trend over box F, the extreme storylines for this box are associated with opposite signs of change in the CP and EP warming indices. In both cases, the extreme wet storyline is associated with a low TW and late $VB_{delay}$ and the extreme dry storyline is associated with the opposite responses, in agreement with the results of M20.

### c. *Decomposing uncertainty: Atmospheric circulation storyline and warming levels*

In this section, we evaluate how uncertainty in large-scale circulation combines with the uncertainty in global warming levels and how the changes estimated using the pattern-scaling assumption deviate from the actual values projected by the models per degree of warming. To do this, we evaluate the

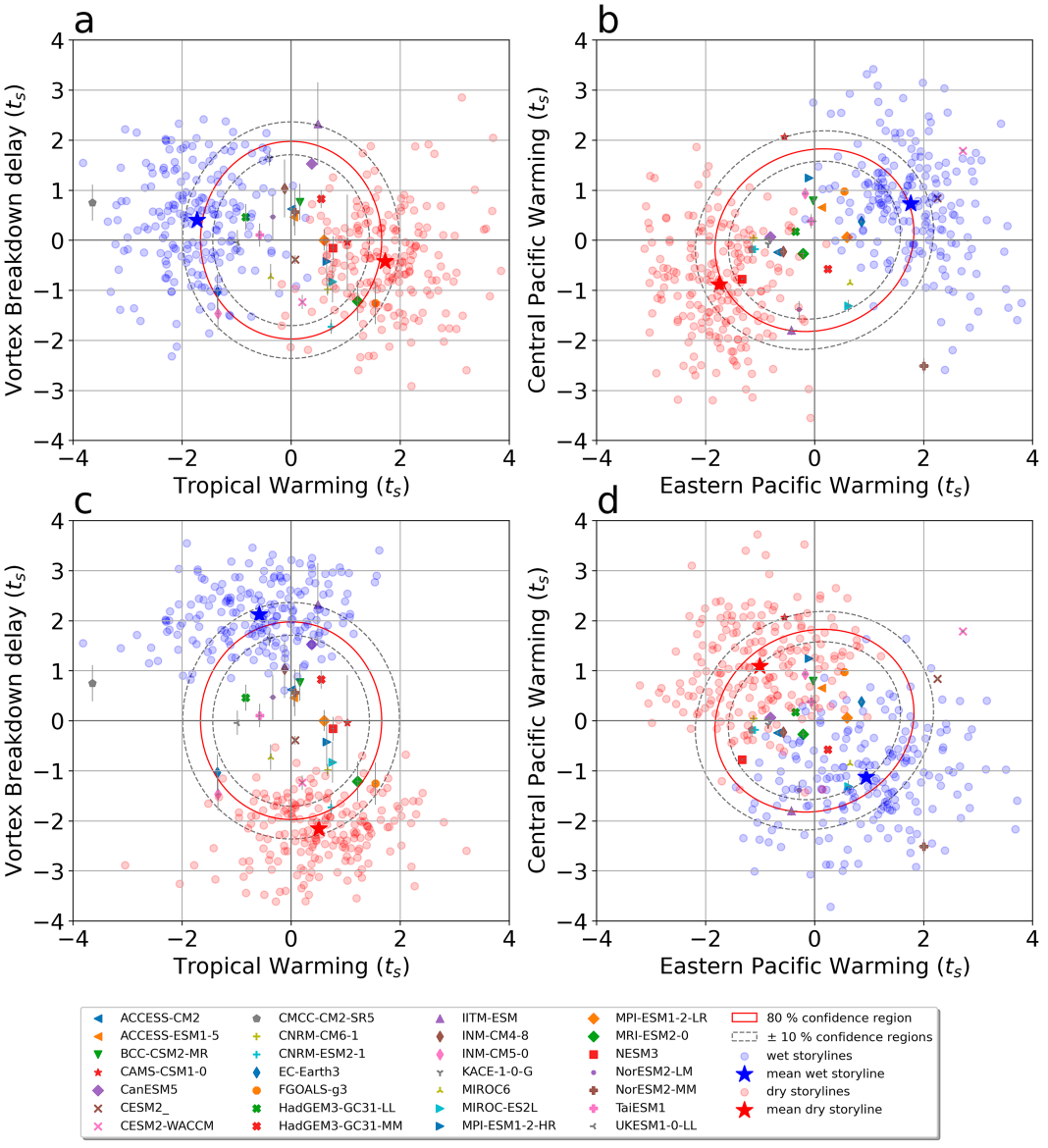


FIG. 11. As in Fig. 7, but for standardized remote driver indices. The overlaid blue and red dots represent the (a) TW and $VB_{delay}$ and (b) CP and EP responses that when combined lead to the extreme storylines in region B in Fig. 1, evaluated as explained in section 4, with blue corresponding to wetting and red to drying. The stars represent the mean remote driver response for the ensemble of extreme storylines. (c),(d) As in (a) and (b), but for region F in Fig. 1.

time by which each warming level is reached in the individual GCM and tabulate the pr changes projected for each time horizon. The precipitation time series were first averaged over the regional boxes and smoothed with a 20-yr moving average filter.

Figure 12 shows each of the model responses per degree of warming. Figures 12a, 12b, and 12c show the pr changes averaged over boxes A (Iturbide et al. 2020), B (M20), and F (Zilli et al. 2017), respectively, in the individual models. The stylized lines (see label in Fig. 12) show the relative contribution of one standard deviation in each remote driver to the pr change in each region. The distance between these lines shows that while CP has a minor contribution to the spread for region F, it plays a significant role for region B. The opposite happens with $VB_{delay}$. The role of TW is comparatively small, while that of EP is non-negligible, for both regions. For region A, which encompasses most of region B and all of region F, these differences are lost and the overall range of pr changes is much smaller. The lines are added with the sign of the change that contributes to wetting (blue) and drying (red) in order to show the extent to which the spread can be covered, and how they deviate from the MEM (black curve); see Fig. 11 and Table 3 for the signs of the remote driver changes in each

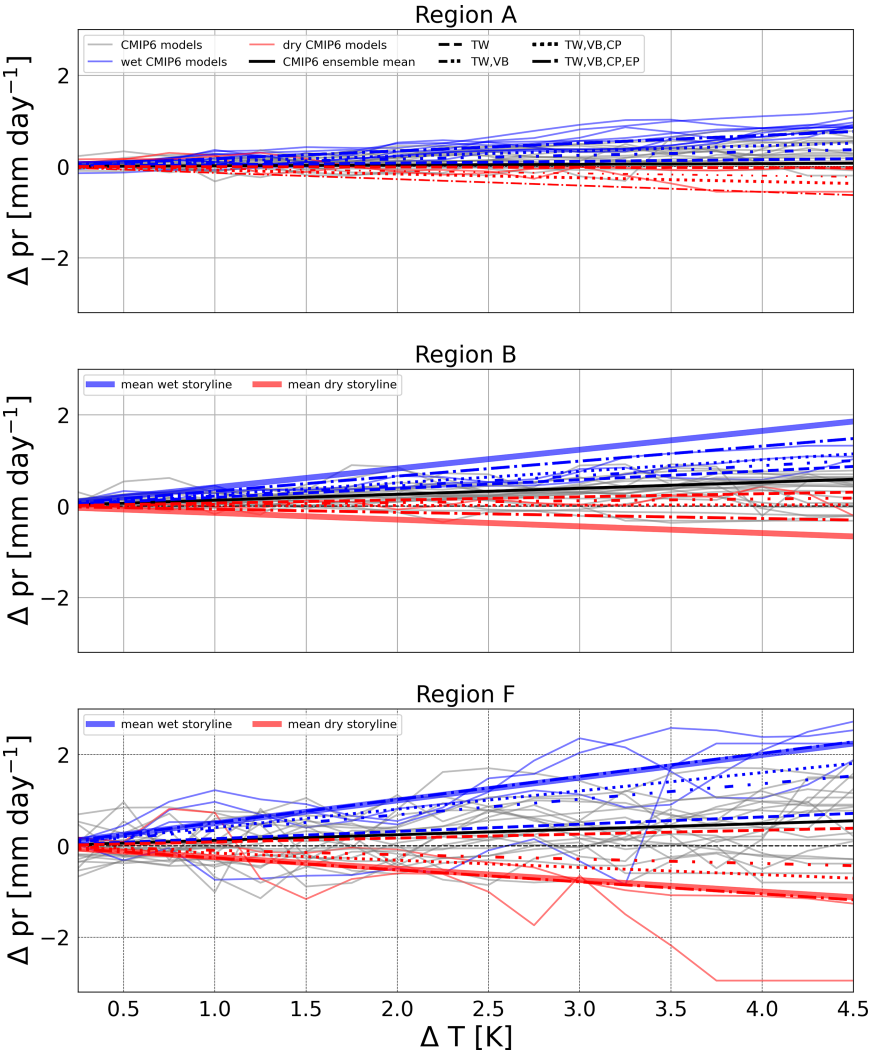


FIG. 12. Pr change as a function of the global warming level ($\Delta T$). Thin solid curves show the individual model responses (gray), with the driest and wettest models colored in red and blue, respectively. Stylized lines show the contribution of each remote driver (see label) to the MEM change (black). Thick solid lines for regions B and F show the mean extreme storylines in Fig. 11 (blue and red stars).

region. The spread in the individual models is almost fully covered by the remote driver responses for boxes A and B, but not for box F, where there is one model (CanESM5) with an extreme dry response. The solid curves show the extreme wet and dry storylines described in the last section (star symbols in Fig. 11).

## 5. Discussion and conclusions

The aim of this work was to understand if the CMIP6 ensemble spread in SE-SA summer precipitation changes can be explained by considering the combined influence of large-scale remote influences that have previously been identified as relevant remote drivers of change in the Southern Hemisphere (SH). To address this aim, we posed the following research questions: (i) Are all of the plausible scenarios for the summer precipitation in SE-SA characterized by wetting conditions only? Are there plausible scenarios involving very weak wetting or even drying? (ii) Can variations in atmospheric circulation patterns forced by large-scale remote drivers explain the differences between contrasting SE-SA precipitation scenarios? (iii) How does one define a regional box for SE-SA that represents the uncertainty in large-scale circulation changes?

Although the MEM shows a wetting response over the regional box in the IPCC WGI report (IPCC 2021) defined as "Southeastern South America (SES)," this response is robust only in a small region within SES (box C in Fig. 1a), and weak wetting and drying changes are also plausible in the remaining areas. The presence of models showing a weak wetting or even a drying trend in the region is enough to argue that drier

conditions in the future cannot be dismissed. What our results additionally show is that there is a combination of remote drivers that can lead to circulation changes with an associated drying response, confirming its plausibility from an atmospheric dynamics perspective. This physical coherence makes the drying response nonnegligible from a risk perspective, even if it is in disagreement with the MEM.

In particular, we found that asymmetric Pacific Ocean SST warming patterns have an important role in shaping future climate in SE-SA and that their spatial influence is not homogeneous over the region. The way in which SST changes are combined with other remote driver responses can lead to a drying response in SE-SA. In particular, if high upper-tropospheric tropical warming and early stratospheric polar vortex breakdown conditions are combined with low central and eastern Pacific warming, this can lead to drying in southern SES (boxes B–E in Fig. 1). Instead, in southeastern Brazil (box F), the drying occurs if high central Pacific warming and low eastern Pacific warming jointly occur. These results answer our first question, confirming that regionalization should be done after addressing the influence of large-scale circulation since spatial averaging can otherwise result in a confounding factor. In addition, they answer the second and third questions pointing out that to fully understand the trends in regional precipitation, a thorough analysis of the underlying physical mechanisms is necessary. We conclude that the direction of summer rainfall changes in SE-SA remains uncertain in CMIP6 and that this uncertainty can in part be explained in terms of different yet plausible large-scale circulation changes. Future work should address how the remote drivers have jointly influenced the large-scale circulation and precipitation in the observed climate trends to better attribute the influence of dynamics in southeastern South America. Moreover, given that it has been recently proposed that a common bias in CMIP models could be leading to a biased warming response in the tropical Pacific, this article shows that given its impacts, the plausibility of an even more extreme storyline in the direction of drying, out of the sampled distribution (Fig. 7), should be evaluated.

In this study, we have employed pattern scaling, which was found to be justifiable for our purposes for a transient scenario (SSP5-8.5) with a fixed time horizon. However, the spatial patterns of circulation and precipitation response to warming are known to be different for transient and equilibrated scenarios (Zappa et al. 2020). Within our storyline framework, the differences between transient and equilibrated scenarios could be represented through differences in the remote driver responses. It would be interesting to investigate the extent to which this could explain the differences in the midlatitude circulation and precipitation responses.

Finally, the results' sensitivity to regionalization when applying the storyline framework shows that this needs to be carefully considered. In fact, we show how regional averaging is a case of Simpson's paradox, a statistical phenomenon that occurs when the presence of an association between variables (e.g., significant correlation) depends on the way that a population is divided into subpopulations. This is a common issue in climate science, and we propose that considering physical patterns related to circulation responses is a way of avoiding aggregating not only over different mean precipitation changes but over different responses in relevant impact variables such as extremes or consecutive numbers of dry days.

*Acknowledgments.* We acknowledge the World Climate Research Programme Working Group on Coupled Modelling, responsible for CMIP, and the modeling groups responsible for producing the simulations. We also thank Neil Hart and two anonymous reviewers for their lucid comments. This study was supported by the UBACyT project 20020130100489BA, the CLIMAX Project funded by Belmont Forum/ANR-15-JCL/-0002-01, and the RECEIPT project funded by EU Horizon 2020 (Grant Agreement 820712). JM is supported by a Ph.D. grant from CONICET, Argentina, and a Microsoft Research Ph.D. Fellowship.

*Data availability statement.* CMIP6 output is available at https://esgf-node.llnl.gov/search/cmip6/. Code is available at https://github.com/jumin94/JoC_asymmetric_sst_patterns.

## APPENDIX A

### Robustness Test

Zappa et al. (2021) proposed a metric to estimate the multimodel ensemble mean of the forced signal-to-noise ratio. The difference from taking the mean of the traditional signal-to-noise ratios ($\gamma_m = |\beta_m/\sigma_m|$, where $\beta_m$ is the mean forced response in the variable and $\sigma_m$ is the year-to-year standard deviation of the variable for model $m$) is that this metric accounts for the contribution of internal variability to the mean change in each model and is thus an unbiased estimator:

$$\gamma_{\text{forced}} = \sqrt{\left(\frac{1}{M}\sum_{m=1}^{M}\frac{\beta_m^2}{\sigma_m^2}\right) - 2\bar{f}}, \tag{A1}$$

where $\bar{f} = \overline{\widehat{\sigma}_m^2}/\overline{\sigma_m^2}$, $\widehat{\sigma}_m^2$ is the variance of the 30-yr mean, the overbar is the multimodel median, and $M$ is the total number of models. The term $\overline{\widehat{\sigma}_m^2}$ is evaluated from the preindustrial simulation, for which all models provide at least 220 years. In Fig. 1, the stippling code is as follows:

- Full stippling: at least 90% of the models agree on the sign of the change
- Open stippling: plausible large response and low model agreement ($\gamma_{\text{forced}} > 1$)
- No stippling: uncertainty in the sign and small signal compared to the year-to-year variability ($\gamma_{\text{forced}} < 1$)

Note that $\sigma_m^2$ could be computed as the variability of the mean, if there are enough samples, which is a metric that is more relevant to show a large climate signal regardless of its impacts. We are interested in the year-to-year variability instead because it represents an estimate for what a population might be currently adapted to.

## APPENDIX B

### Storyline Evaluation

To emulate the storylines shown in section 4, we estimate the distribution of standardized remote driver responses scaled by global warming as a multivariate normal distribution, which requires evaluating the covariance matrix ($\boldsymbol{\Sigma}$) that describes how the remote drivers vary together (after scaling by global warming). Each remote driver was treated as a normally distributed random variable and the correlations among remote drivers (small in the case of this study) were also considered, meaning that the approach can consider the effects of common drivers leading to remote driver correlations.

The probability density function (PDF) of a multivariate normal distribution is given by

$$f(\mathbf{x}) = \frac{\exp\left[-\frac{1}{2}(\mathbf{x}-\boldsymbol{\mu})^{\mathrm{T}}\boldsymbol{\Sigma}^{-1}(\mathbf{x}-\boldsymbol{\mu})\right]}{\sqrt{(2\pi)^k\,|\boldsymbol{\Sigma}|}} \tag{B1}$$

where $\mathbf{x}$ is a $k$-dimensional random variable, $\boldsymbol{\mu}$ is the mean vector, $\boldsymbol{\Sigma}$ is the covariance matrix, and $|\boldsymbol{\Sigma}|$ is the determinant of $\boldsymbol{\Sigma}$. A univariate Gaussian distribution is used to sample the global warming level.

For each storyline, a vector of remote driver responses is sampled ($[t_{\mathrm{TW}}, t_{\mathrm{VB}}, t_{\mathrm{CP}}, t_{\mathrm{EP}}]$), and independently, a value of global warming level is sampled ($t_{\mathrm{GW}}$). The precipitation change under each storyline is evaluated as

$$\Delta C_{\mathrm{SL}} = (a_x + b_x t_{\mathrm{TW}} + c_x t_{\mathrm{VB}} + d_x t_{\mathrm{CP}} + e_x t_{\mathrm{EP}}) t_{\mathrm{GW}}, \tag{B2}$$

where $a_x$, $b_x$, $c_x$, $d_x$, and $e_x$ are the MLR regression coefficients. The values of SL in Fig. 10a are evaluated with (B2), and the values of SL in Figs. 8b and 10b are evaluated with the term in parentheses only.

## REFERENCES


Almazroui, M., and Coauthors, 2021: Assessment of CMIP6 performance and projected temperature and precipitation changes over South America. *Earth Syst. Environ.*, **5**, 155–183, https://doi.org/10.1007/s41748-021-00233-6.

Barros, V., M. Gonzalez, B. Liebmann, and I. Camilloni, 2000: Influence of the South Atlantic convergence zone and South Atlantic sea surface temperature on interannual summer rainfall variability in southeastern South America. *Theor. Appl. Climatol.*, **67**, 123–133, https://doi.org/10.1007/s007040070002.

Berbery, E. H., and C. S. Vera, 1996: Characteristics of the Southern Hemisphere winter storm track with filtered and unfiltered data. *J. Atmos. Sci.*, **53**, 468–481, https://doi.org/10.1175/1520-0469(1996)053<0468:COTSHW>2.0.CO;2.

Breul, P., P. Ceppi, and T. G. Shepherd, 2023: Revisiting the wintertime emergent constraint of the Southern Hemispheric midlatitude jet response to global warming. *Wea. Climate Dyn.*, **4**, 39–47, https://doi.org/10.5194/wcd-4-39-2023.

Butler, A. H., D. W. Thompson, and R. Heikes, 2010: The steady-state atmospheric circulation response to climate change-like thermal forcings in a simple general circulation model. *J. Climate*, **23**, 3474–3496, https://doi.org/10.1175/2010JCLI3228.1.

Byrne, N. J., and T. G. Shepherd, 2018: Seasonal persistence of circulation anomalies in the Southern Hemisphere stratosphere and its implications for the troposphere. *J. Climate*, **31**, 3467–3483, https://doi.org/10.1175/JCLI-D-17-0557.1.

Ceppi, P., and T. G. Shepherd, 2019: The role of the stratospheric polar vortex for the austral jet response to greenhouse gas forcing. *Geophys. Res. Lett.*, **46**, 6972–6979, https://doi.org/10.1029/2019GL082883.

Cortés, J., M. Mahecha, M. Reichstein, and A. Brenning, 2020: Accounting for multiple testing in the analysis of spatio-temporal environmental data. *Environ. Ecol. Stat.*, **27**, 293–318, https://doi.org/10.1007/s10651-020-00446-4.

Díaz, L. B., R. I. Saurral, and C. S. Vera, 2021: Assessment of South America summer rainfall climatology and trends in a set of global climate models large ensembles. *Int. J. Climatol.*, **41**, E59–E77, https://doi.org/10.1002/joc.6643.

Doblas-Reyes, F. J., and Coauthors, 2021: Linking global to regional climate change. *Climate Change 2021: The Physical Science Basis*, V. Masson-Delmotte, et al., Eds., Cambridge University Press, 1363–1512, https://doi.org/10.1017/9781009157896.012.

Doyle, M. E., and V. R. Barros, 2002: Midsummer low-level circulation and precipitation in subtropical South America and related sea surface temperature anomalies in the South Atlantic. *J. Climate*, **15**, 3394–3410, https://doi.org/10.1175/1520-0442(2002)015<3394:MLLCAP>2.0.CO;2.

Elbaum, E., C. I. Garfinkel, O. Adam, E. Morin, D. Rostkier-Edelstein, and U. Dayan, 2022: Uncertainty in projected changes in precipitation minus evaporation: Dominant role of dynamic circulation changes and weak role for thermodynamic changes. *Geophys. Res. Lett.*, **49**, e2022GL097725, https://doi.org/10.1029/2022GL097725.

Eyring, V., S. Bony, G. A. Meehl, C. A. Senior, B. Stevens, R. J. Stouffer, and K. E. Taylor, 2016: Overview of the Coupled Model Intercomparison Project phase 6 (CMIP6) experimental design and organization. *Geosci. Model Dev.*, **9**, 1937–1958, https://doi.org/10.5194/gmd-9-1937-2016.

Gonzalez, P. L. M., L. M. Polvani, R. Seager, and G. J. P. Correa, 2014: Stratospheric ozone depletion: A key driver of recent precipitation trends in south eastern South America. *Climate Dyn.*, **42**, 1775–1792, https://doi.org/10.1007/s00382-013-1777-x.

Grimm, A. M., V. R. Barros, and M. E. Doyle, 2000: Climate variability in southern South America associated with El Niño and La Niña events. *J. Climate*, **13**, 35–58, https://doi.org/10.1175/1520-0442(2000)013%3C0035:CVISSA%3E2.0.CO;2.

Hodnebrog, Ø., B. M. Steensen, L. Marelle, K. Alterskjær, S. B. Dalsøren, and G. Myhre, 2022: Understanding model diversity in future precipitation projections for South America. *Climate Dyn.*, **58**, 1329–1347, https://doi.org/10.1007/s00382-021-05964-w.

IPCC, 2021: *Climate Change 2021: The Physical Science Basis*. Cambridge University Press, https://doi.org/10.1017/9781009157896.

Iturbide, M., and Coauthors, 2020: An update of IPCC climate reference regions for subcontinental analysis of climate model data: Definition and aggregated datasets. *Earth Syst. Sci. Data*, **12**, 2959–2970, https://doi.org/10.5194/essd-12-2959-2020.

Jones, C., 2019: Recent changes in the South America low-level jet. *npj Climate Atmos. Sci.*, **2**, 20, https://doi.org/10.1038/s41612-019-0077-5.

Jones, P. W., 1999: First- and second-order conservative remapping schemes for grids in spherical coordinates. *Mon. Wea. Rev.*, **127**, 2204–2210, https://doi.org/10.1175/1520-0493(1999)127<2204:FASOCR>2.0.CO;2.

Junquas, C., C. Vera, L. Li, and H. Le Treut, 2012: Summer precipitation variability over southeastern South America in a global warming scenario. *Climate Dyn.*, **38**, 1867–1883, https://doi.org/10.1007/s00382-011-1141-y.

——, ——, ——, and ——, 2013: Impact of projected SST changes on summer rainfall in southeastern South America. *Climate Dyn.*, **40**, 1569–1589, https://doi.org/10.1007/s00382-013-1695-y.

Kidson, J. W., 1988: Indices of the Southern Hemisphere zonal wind. *J. Climate*, **1**, 183–194, https://doi.org/10.1175/1520-0442(1988)001<0183:IOTSHZ>2.0.CO;2.

Knutti, R., D. Masson, and A. Gettelman, 2013: Climate model genealogy: Generation CMIP5 and how we got there. *Geophys. Res. Lett.*, **40**, 1194–1199, https://doi.org/10.1002/grl.50256.

Lee, J.-Y., and Coauthors, 2021: Future global climate: Scenario-based projections and near-term information. *Climate Change 2021: The Physical Science Basis*, V. Masson-Delmotte et al., Eds., 553–672, Cambridge University Press, https://doi.org/doi:10.1017/9781009157896.006.

Lee, S., M. L'Heureux, A. T. Wittenberg, R. Seager, P. A. O'Gorman, and N. C. Johnson, 2022: On the future zonal contrasts of equatorial Pacific climate: Perspectives from observations, simulations, and theories. *npj Climate Atmos. Sci.*, **5**, 82, https://doi.org/10.1038/s41612-022-00301-2.

Manzini, E., and Coauthors, 2014: Northern winter climate change: Assessment of uncertainty in CMIP5 projections related to stratosphere–troposphere coupling. *J. Geophys. Res. Atmos.*, **119**, 7979–7998, https://doi.org/10.1002/2013JD021403.

Martín-Gómez, V., M. Barreiro, and E. Mohino, 2020: Southern Hemisphere sensitivity to ENSO patterns and intensities: Impacts over subtropical South America. *Atmosphere*, **11**, 77, https://doi.org/10.3390/atmos11010077.

McKay, R. C., and Coauthors, 2023: Can southern Australian rainfall decline be explained? A review of possible drivers. *Wiley Interdiscip. Rev.: Climate Change*, **14**, e820, https://doi.org/10.1002/wcc.820.

Mindlin, J., T. G. Shepherd, C. S. Vera, M. Osman, G. Zappa, R. W. Lee, and K. I. Hodges, 2020: Storyline description of Southern Hemisphere midlatitude circulation and precipitation response to greenhouse gas forcing. *Climate Dyn.*, **54**, 4399–4421, https://doi.org/10.1007/s00382-020-05234-1.

——, ——, ——, and ——, 2021: Combined effects of global warming and ozone depletion/recovery on Southern Hemisphere atmospheric circulation and regional precipitation. *Geophys. Res. Lett.*, **48**, e2021GL092568, https://doi.org/10.1029/2021GL092568.

Mo, K. C., and R. W. Higgins, 1998: The Pacific-South American modes and tropical convection during the Southern Hemisphere winter. *Mon. Wea. Rev.*, **126**, 1581–1596, https://doi.org/10.1175/1520-0493(1998)126%3C1581:TPSAMA%3E2.0.CO;2.

——, and J. N. Paegle, 2001: The Pacific-South American modes and their downstream effects. *Int. J. Climatol.*, **21**, 1211–1229, https://doi.org/10.1002/joc.685.

Montini, T. L., C. Jones, and L. M. V. Carvalho, 2019: The South American low-level jet: A new climatology, variability, and changes. *J. Geophys. Res. Atmos.*, **124**, 1200–1218, https://doi.org/10.1029/2018JD029634.

Nguyen, H., H. H. Hendon, E.-P. Lim, G. Boschat, E. Maloney, and B. Timbal, 2018: Variability of the extent of the Hadley circulation in the Southern Hemisphere: A regional perspective. *Climate Dyn.*, **50**, 129–142, https://doi.org/10.1007/s00382-017-3592-2.

Pfahl, S., P. A. O'Gorman, and E. M. Fischer, 2017: Understanding the regional pattern of projected future changes in extreme precipitation. *Nat. Climate Change*, **7**, 423–427, https://doi.org/10.1038/nclimate3287.

Reboita, M. S., M. A. Gan, R. P. da Rocha, and T. Ambrizzi, 2010: Precipitation regimes in South America: A bibliography review. *Rev. Bras. Meteor.*, **25**, 185–204, https://doi.org/10.1590/S0102-77862010000200004.

——, T. Ambrizzi, B. A. Silva, R. F. Pinheiro, and R. P. da Rocha, 2019: The South Atlantic subtropical anticyclone: Present and future climate. *Front. Earth Sci.*, **7**, 8, https://doi.org/10.3389/feart.2019.00008.

Saurral, R. I., I. A. Camilloni, and V. R. Barros, 2017: Low-frequency variability and trends in centennial precipitation stations in southern South America. *Int. J. Climatol.*, **37**, 1774–1793, https://doi.org/10.1002/joc.4810.

Schlindwein, S. L., A. C. Feitosa de Vasconcelos, M. Bonatti, S. Sieber, A. Strapasson, and M. Lana, 2021: Agricultural land use dynamics in the Brazilian part of La Plata Basin: From driving forces to societal responses. *Land Use Policy*, **107**, 105519, https://doi.org/10.1016/j.landusepol.2021.105519.

Schmidt, D. F., and K. M. Grise, 2017: The response of local precipitation and sea level pressure to Hadley cell expansion. *Geophys. Res. Lett.*, **44**, 10 573–10 582, https://doi.org/10.1002/2017GL075380.

Shepherd, T. G., 2014: Atmospheric circulation as a source of uncertainty in climate change projections. *Nat. Geosci.*, **7**, 703–708, https://doi.org/10.1038/ngeo2253.

Silvestri, G., and C. Vera, 2009: Nonstationary impacts of the Southern Annular Mode on Southern Hemisphere climate. *J. Climate*, **22**, 6142–6148, https://doi.org/10.1175/2009JCLI3036.1.

Takaya, K., and H. Nakamura, 2001: A formulation of a phase-independent wave-activity flux for stationary and migratory quasigeostrophic eddies on a zonally varying basic flow. *J. Atmos. Sci.*, **58**, 608–627, https://doi.org/10.1175/1520-0469(2001)058<0608:AFOAPI>2.0.CO;2.

Tebaldi, C., and J. M. Arblaster, 2014: Pattern scaling: Its strengths and limitations, and an update on the latest model simulations. *Climatic Change*, **122**, 459–471, https://doi.org/10.1007/s10584-013-1032-9.

van Garderen, L., and J. Mindlin, 2022: A storyline attribution of the 2011/2012 drought in southeastern South America. *Weather*, **77**, 212–218, https://doi.org/10.1002/wea.4185.

Vera, C. S., and L. Díaz, 2015: Anthropogenic influence on summer precipitation trends over South America in CMIP5 models. *Int. J. Climatol.*, **35**, 3172–3177, https://doi.org/10.1002/joc.4153.

Wilks, D. S., 2016: "The stippling shows statistically significant grid points": How research results are routinely overstated and overinterpreted, and what to do about it. *Bull. Amer. Meteor. Soc.*, **97**, 2263–2273, https://doi.org/10.1175/BAMS-D-15-00267.1.

Wu, Y., and L. M. Polvani, 2015: Contrasting short- and long-term projections of the hydrological cycle in the southern extratropics. *J. Climate*, **28**, 5845–5856, https://doi.org/10.1175/JCLI-D-15-0040.1.

Yang, Y.-M., J.-H. Park, S.-I. An, B. Wang, and X. Luo, 2021: Mean sea surface temperature changes influence ENSO-related precipitation changes in the mid-latitudes. *Nat. Commun.*, **12**, 1495, https://doi.org/10.1038/s41467-021-21787-z.

Zak, M. R., M. Cabido, D. Cáceres, and S. Díaz, 2008: What drives accelerated land cover change in central Argentina? Synergistic consequences of climatic, socioeconomic, and technological factors. *Environ. Manage.*, **42**, 181–189, https://doi.org/10.1007/s00267-008-9101-y.

Zappa, G., and T. G. Shepherd, 2017: Storylines of atmospheric circulation change for European regional climate impact assessment. *J. Climate*, **30**, 6561–6577, https://doi.org/10.1175/JCLI-D-16-0807.1.

——, P. Ceppi, and T. G. Shepherd, 2020: Time-evolving sea-surface warming patterns modulate the climate change response of subtropical precipitation over land. *Proc. Natl. Acad. Sci. USA*, **117**, 4539–4545, https://doi.org/10.1073/pnas.1911015117.

——, E. Bevacqua, and T. G. Shepherd, 2021: Communicating potentially large but non-robust changes in multi-model projections of future climate. *Int. J. Climatol.*, **41**, 3657–3669, https://doi.org/10.1002/joc.7041.

Zilli, M. T., L. M. V. Carvalho, B. Liebmann, and M. A. Silva Dias, 2017: A comprehensive analysis of trends in extreme precipitation over southeastern coast of Brazil. *Int. J. Climatol.*, **37**, 2269–2279, https://doi.org/10.1002/joc.4840.

——, ——, and B. R. Lintner, 2019: The poleward shift of South Atlantic convergence zone in recent decades. *Climate Dyn.*, **52**, 2545–2563, https://doi.org/10.1007/s00382-018-4277-1.